(Received 16 February 2026, Accepted 16 March 2026, Scheduled 12 April 2026)

Deep Learning Enabled Inverse Design of Angular-Selective Metasurface Absorbers

Zheng Zhen[1, 2, 3], Kai Wang[1, 2, 3], Haomin Wang[1, 2, 3], Caofei Luo[1, 2, 3], Zhicheng Pei[1, 2, 3], Huan Lu[1, 2, 3, *], and Bin Zheng[1, 2, 3]

[1] *Interdisciplinary Center for Quantum Information, State Key Laboratory of Modern Optical Instrumentation ZJU-Hangzhou Global Scientific and Technological Innovation Center, Zhejiang University, Hangzhou 310027, China*
[2] *International Joint Innovation Center, Key Laboratory of Advanced Micro/Nano Electronic Devices & Smart Systems of Zhejiang The Electromagnetics Academy at Zhejiang University, Zhejiang University, Haining 314400, China*
[3] *Jinhua Institute of Zhejiang University, Zhejiang University, Jinhua 321099, China*

ABSTRACT: This work presents deep neural networks for the inverse design of an ITO-film angular-selective metasurface absorber. A tandem deep neural network (T-DNN) framework is developed for the inverse design of electromagnetic metasurfaces. A forward network is first trained independently to learn the complex physical mapping between metasurface structures and their electromagnetic responses. An inverse network is then trained in tandem with the pre-trained forward network, eliminating conventional parameter-by-parameter tuning and establishing a performance-driven pipeline that directly maps target electromagnetic responses to structural parameters. Using the trained network, several metasurface absorbers with distinct angular sensitivities are rapidly designed, and their angle-dependent applications are preliminarily investigated. Results show that deep learning enables the fast design of metasurface absorbers customized to realistic incident angle distributions, yielding efficient omnidirectional radar cross-section (RCS) reduction at sensitive angles. This work offers a new strategy for the fast design of omnidirectional scattering suppression.

1. INTRODUCTION

In recent years, the rapid proliferation of wireless communication devices has profoundly transformed human life and work. These advancements bring remarkable convenience and efficiency, but the large-scale deployment of electronic and radio-frequency equipment has also introduced critical challenges. The most notable among them is the escalating electromagnetic radiation and interference, which not only poses potential risks to human health but also disrupts the operation of precision instruments and compromises the stability of communication systems [1].

Against this backdrop, electromagnetic absorption technology has emerged as a key research area in both academia and industry. As an effective solution to mitigate electromagnetic pollution and interference, electromagnetic absorbers have attracted wide attention. Through rational material selection and structural design, these devices can absorb or shield electromagnetic waves to minimize adverse effects. Initially driven by defense needs in stealth technology, electromagnetic absorbers now find applications across a broad spectrum of civilian and military domains. They are critical to national security interests, such as military stealth and electronic countermeasures, while also playing pivotal roles in electromagnetic compatibility, radiation protection, biomedical sensing, information transmission, and renewable energy systems [2]. Furthermore, electromagnetic absorption technology holds substantial promise in emerging fields, including detection, imaging, and sensing, which fosters continuous innovation and interdisciplinary integration.

Conventional electromagnetic absorbers, however, are often constrained by the intrinsic properties of their constituent materials. They suffer from limitations such as large volume, excessive weight, high cost, inadequate environmental stability, and limited design flexibility [3]. Developing lightweight, high-performance, and adaptive electromagnetic absorbing materials and structures has thus become an important research goal.

Metamaterials are artificially engineered three-dimensional composite electromagnetic structures. By precisely tailoring the dimensions, geometry, arrangement, and material parameters of their unit cells, metamaterials can achieve electromagnetic responses that are unattainable with natural materials. This enables effective control over electromagnetic waves [4]. Since their conception, metamaterials have attracted sustained interest, leading to the development of structures with exotic properties, including left-handed materials, single-negative materials, and near-zero-index materials [5–8]. These structures have demonstrated significant potential in photonic crystals, perfect lenses, and electromagnetic cloaking.

Metasurfaces are the two-dimensional planar counterparts of metamaterials. They consist of artificially engineered electromagnetic unit cells arranged periodically or aperiodically at subwavelength scales, and they enable efficient manipulation of the amplitude, phase, and polarization of incident electromagnetic waves within a compact footprint [9]. While retaining the flexible wavefront engineering capabilities of tra-

* Corresponding author: Huan Lu (luhuan123@zju.edu.cn).

ditional metamaterials, metasurfaces offer additional advantages. These include a low profile, ease of integration, high electromagnetic tunability through patterned unit cell design, and reduced fabrication complexity and cost compared to three-dimensional metamaterials. These attributes render metasurfaces amenable to large-scale production and practical applications, establishing them as a research hotspot in the field of electromagnetic functional materials [10–13].

With the rapid advancement of metasurface technology, its application in electromagnetic absorption has garnered increasing attention. It offers a pathway to overcome the limitations of conventional absorbers such as large volume, narrow bandwidth, and limited tunability. In 2008, Landy et al. proposed the first perfect metasurface absorber based on a metal-dielectric-metal composite structure, which inaugurated this research direction [14]. Subsequent progress has witnessed advancements in material systems, structural design, and functionality. Fabrication processes have been streamlined; all-dielectric configurations have emerged; absorption characteristics have evolved from single-frequency to multi-frequency and broadband operation; and operational frequencies have expanded from microwave to terahertz and infrared ranges [15–17]. For instance, Ding et al. achieved broadband, high-efficiency absorption in the 7.8–14.7 GHz band using a multilayer conical pyramid structure [18]. Zhang et al. demonstrated dynamic switching between absorption and reflection states using PIN diodes [19]. Zhu et al. proposed an all-dielectric coherent absorber that enables reconfigurable control over absorption magnitude and operating frequency [20].

Despite these advances, metasurface absorbers still face a critical bottleneck for practical deployment. Their absorption performance degrades significantly as the incident angle increases, and this observation motivates this work. Instead of treating angular sensitivity as an inherent flaw, we integrate it into the design strategy. By integrating unit cells optimized for high absorption at specific incident angles, we aim to enhance overall angular robustness. The core challenge, however, lies in designing such angle-sensitive unit cells efficiently. Conventional approaches rely heavily on designer expertise, combining commercial simulation software with manual parameter tuning and trial-and-error iterations. This process is time-consuming and inefficient, and it is unable to efficiently meet diverse and complex performance requirements.

In recent years, machine learning has greatly advanced metamaterial design methodologies. Deep learning and optimization techniques are widely adopted for unit cell design [21–23], which has led to the emergence of adaptive intelligent metamaterial systems [24–28]. Numerous studies have demonstrated the utility of machine learning in inverse design and structural optimization of metasurface unit cells. For example, tandem neural networks have been employed to optimize metasurface arrangements for transmissive cloaking applications [29]. Meanwhile, advances in reconfigurable metasurface hardware combined with the data processing capabilities of deep learning have enabled adaptive electromagnetic processing systems. One such example is systems that respond to incident wave characteristics in real time to achieve adaptive cloaking for vehicles [30]. These techniques greatly reduce design complexity and associated costs.

In this paper, we propose a metasurface absorber based on indium tin oxide resistive films and investigate its inverse design using deep learning. We explore the angular-sensitive characteristics of the absorber and their potential applications, detail the design principles and implementation workflow of a tandem deep neural network for metasurface inverse design, and optimize key hyperparameters to construct a problem-specific tandem deep neural network (T-DNN). Model validity is confirmed through test set evaluation and full-wave simulations. Leveraging the trained network, we inversely design two types of metasurface absorbers that exhibit distinct angular sensitivity characteristics for non-planar configurations. Simulation results demonstrate enhanced absorption performance achieved through their strategic integration. This work provides a general and efficient deep-learning-driven inverse design framework for angularly robust metasurface absorbers.

2. ANGULAR-SELECTIVE METASURFACE ABSORBERS

We proposed a novel metasurface absorber unit cell, as shown in Fig. 1. Its angular-dependent electromagnetic response was investigated to support inverse design and scattering applications. The unit cell comprises three functional layers. The top layer is a centered solid octagonal pattern made of indium tin oxide (ITO) film, supported by a flexible polyethylene terephthalate (PET) substrate. The middle layer is an ITO film patterned as either a concentric octagonal ring or a solid octagon, also supported by a PET substrate. The bottom layer is a metallic ground plane that completely reflects incident electromagnetic waves, thereby enhancing absorption. The structural parameters are defined as follows: $R1$ denotes the circumscribed circle radius of the top octagon, ranging from 1 mm to $(P-1)/2$ mm; $R2$ and $R3$ represent the outer and inner circumscribed circle radii of the middle concentric annular octagon, with $1 \leq R3 < R2 \leq (P-1)/2$ mm; P is the side length of

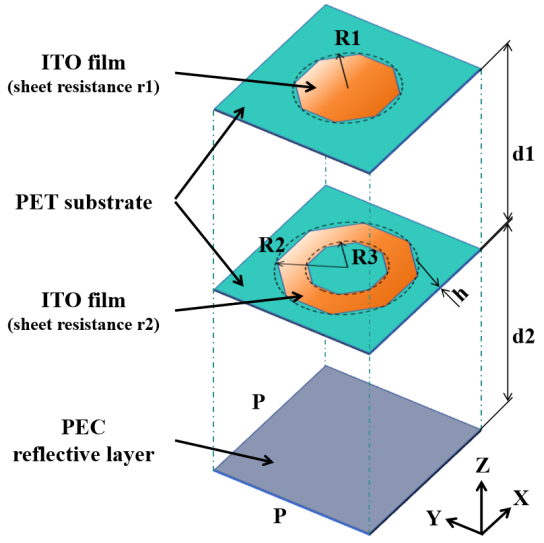

FIGURE 1. Schematic of metasurfaces absorber model.

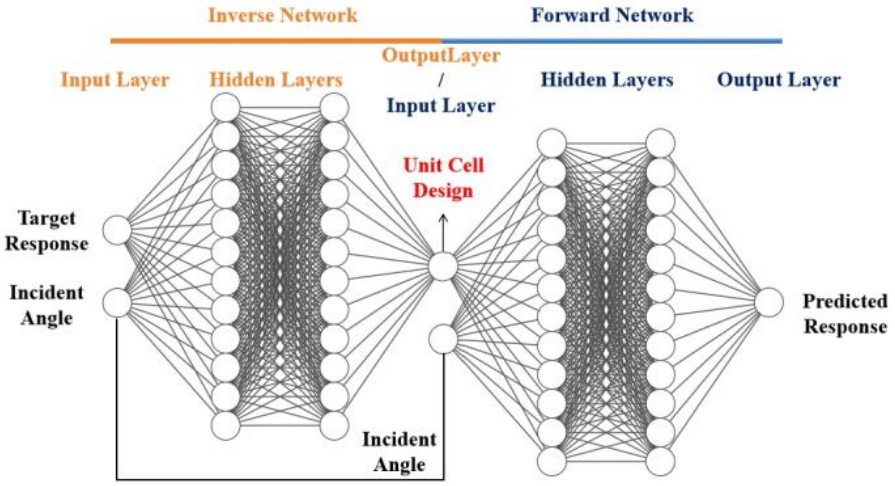

FIGURE 2. Tandem deep neural network, T-DNN.

the unit cell (periodicity), ranging from 10 mm to 20 mm; h is the thickness of the PET substrate (0.188 mm). The three layers are separated by air gaps, with $d1$ between the top and middle layers and $d2$ between the middle and bottom layers (both $d1 = d2 = 3$ mm). For material properties, the sheet resistance $r1 = r2$ of each ITO film varies from 10 Ω/sq to 100 Ω/sq. The relative permittivity of the PET substrate is $\varepsilon_{PET} = 3$. The metallic ground plane is modeled as a perfect electric conductor in simulations. By appropriately designing the structural dimensions and material parameters, the absorption performance can be tailored across different frequencies and incident angles.

To thoroughly analyze the absorption performance of the proposed unit cell, full-wave electromagnetic simulations were conducted using Computer Simulation Technology (CST) Studio Suite. The absorption $A(\omega)$ of the metasurface absorber is determined by both the reflection coefficient $R(\omega)$ and transmission coefficient $T(\omega)$, and is defined as:

$$A(\omega) = 1 - R(\omega) - T(\omega) \tag{1}$$

$$A(\omega) = 1 - |S_{11}|^2 - |S_{21}|^2 \tag{2}$$

where S_{11} and S_{21} are the reflection and transmission coefficients, respectively. Due to the presence of the metallic ground plane, incident electromagnetic waves are completely reflected at the bottom layer, making transmission negligible ($T(\omega) \approx 0$). The absorptivity can be simplified to:

$$A(\omega) = 1 - R(\omega) = 1 - |S_{11}|^2 \tag{3}$$

The absorption performance was evaluated by calculating the absorption from the simulated reflection coefficients S_{11}. Angular sensitivity was investigated by comparing the simulation results obtained under different incident angles, thereby analyzing the absorption behavior under oblique illumination.

Due to the geometric symmetry of the proposed unit cell along the x- and y-axes, the structure exhibits identical electromagnetic responses under x-polarized and y-polarized incidences. Therefore, the designed absorber is inherently polarization-insensitive, and the absorption performance discussed above holds for both polarizations.

In this work, periodic boundary conditions were applied in the x and y directions. Open boundary conditions were used in the z direction. The frequency range was set from 6 GHz to 12 GHz.

3. INVERSE DESIGN BASED ON TANDEM DEEP NEURAL NETWORK

To achieve efficient inverse design of the metasurface absorber, an effective method based on a tandem deep neural network was introduced. The full workflow is presented in Fig. 2.

3.1. T-DNN Design Workflow

The key steps in the design of T-DNN are as follows.

3.1.1. Datasets Generation

To train the T-DNN model, datasets with sufficient samples were constructed. The input data comprises structural and material parameters of the metasurface absorber, including the unit cell period, geometric pattern parameters, and sheet resistance. The corresponding output data consists of the electromagnetic response, specifically the S_{11} curves.

Parameter combinations were generated through quasi-random sampling in the parameter space. For each parameter combination, full-wave simulations were performed to obtain the S_{11} data, yielding 45,000 samples. These samples were randomly divided into three subsets: 70% for training, 15% for validation, and the remaining 15% for testing.

3.1.2. Datasets Preprocessing

Before constructing the network model and initiating training, normalization preprocessing was applied so that all feature parameters share the same order of magnitude, thereby improving convergence speed and prediction accuracy.

In this work, the S_{11} parameter in dB was converted to linear values, and the absorption was calculated according to formula (3) as a form of standardization. This compression behavior

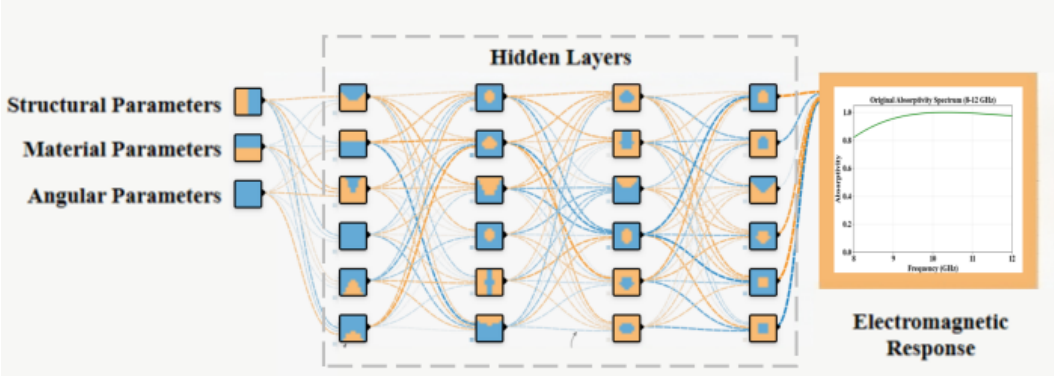

FIGURE 3. Forward prediction DNN.

aligns with practical application requirements for electromagnetic response while improving data distribution robustness.

3.1.3. Forward Prediction Network Training

A deep neural network was designed for the forward prediction task and trained independently using the forward prediction datasets. The network takes structural and material parameters as input and outputs the corresponding electromagnetic response curves.

During training, the mean squared error was adopted as the loss function to quantify the discrepancy between predicted and actual curves:

$$MSE = \frac{1}{n}\sum_{i=1}^{n}(y_i - \hat{y}_i)^2 \tag{4}$$

where y_i is the ground truth output, and $\hat{y}_i$ is the network prediction. To prevent overfitting, L2 regularization was introduced, and early stopping was employed to monitor the training process.

3.1.4. Inverse Design Network Training

The inverse design network also adopts a DNN structure, but it must be trained in tandem with the pre-trained forward network. Specifically, the output of the inverse network is connected to the input of the forward network, and the parameters of the forward network are frozen during training. The tandem network is then trained using the inverse design datasets.

The input to the tandem network consists of angular-sensitive parameters (incident angle) and the target electromagnetic response, while the output is the predicted electromagnetic response. The designed structural parameters are obtained from the output of the inverse network. MSE is again used as the loss function to measure the discrepancy between the predicted and target curves.

3.1.5. Inverse Design of Angular-Selective Metasurface Absorbers

By inputting a set of parameters (incident angle and target electromagnetic response), the trained inverse network rapidly generates the required structural and material parameters. The forward network then predicts the corresponding electromagnetic response.

3.2. Forward Prediction Deep Neural Network

Inverse design based on electromagnetic responses faces a key challenge. Structures with significantly different parameters can yield comparable or even identical responses in the target frequency band. This phenomenon of similar solutions often complicates the design process. When an inverse network is used alone, such data with similar inputs but varying output labels can confuse the network during training, adversely affecting both learning accuracy and convergence speed. Moreover, in engineering practice, the actual performance of the inversely designed unit cell is the ultimate design goal, rather than confining parameter selection within the dataset's space. Introducing a forward network shifts the evaluation from parameter design directly to performance assessment, which better aligns with practical engineering needs and facilitates parameter generalization for optimal solutions.

The forward prediction DNN model is shown in Fig. 3. The network consists of an input layer, 4 hidden layers (each containing 512 neurons), and an output layer. Each layer contains numerous neurons that are fully connected to the next layer, with connection weights continuously updated during training.

The network input includes structural parameters $(P, R1, R2, R3)$, material parameters $(r1, r2)$, and angle parameters (incident angle θ). The output is the corresponding electromagnetic response (absorption performance).

The loss curve during forward network training is shown in Fig. 4(a). As the number of iterations increases, the loss function begins to decrease. When the downward trend stagnates, the network automatically reduces the learning rate and continues training until the loss function stops decreasing, or the maximum number of iterations is reached.

The final test loss reached 0.0012. Several metasurface absorber unit cells were randomly selected from the test set, and their parameters were fed into the forward network. The predicted results were compared with full-wave simulation results, as shown in Fig. 5. The forward network accurately predicts the absorption performance (electromagnetic response) of several unit cells under different incident angles. Whether the absorp-

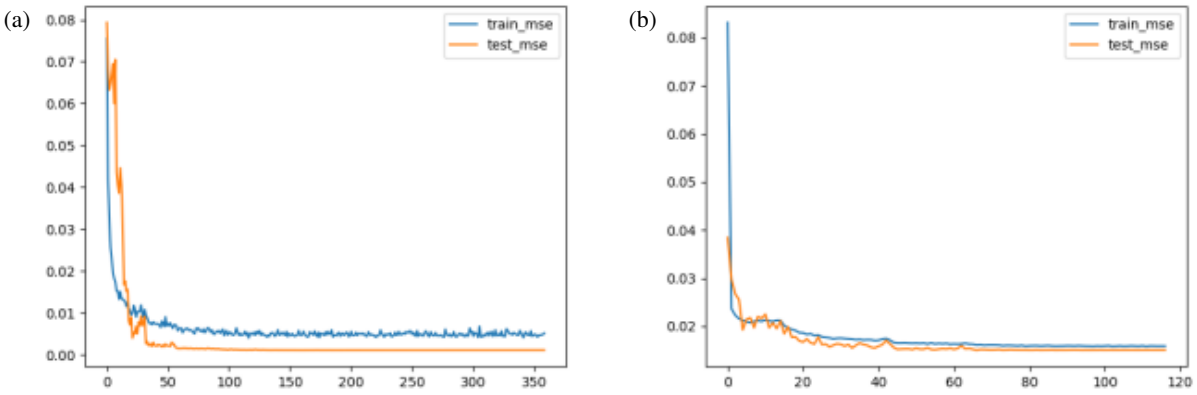

FIGURE 4. Learning performance of (a) forward prediction DNN and (b) inverse design DNN.

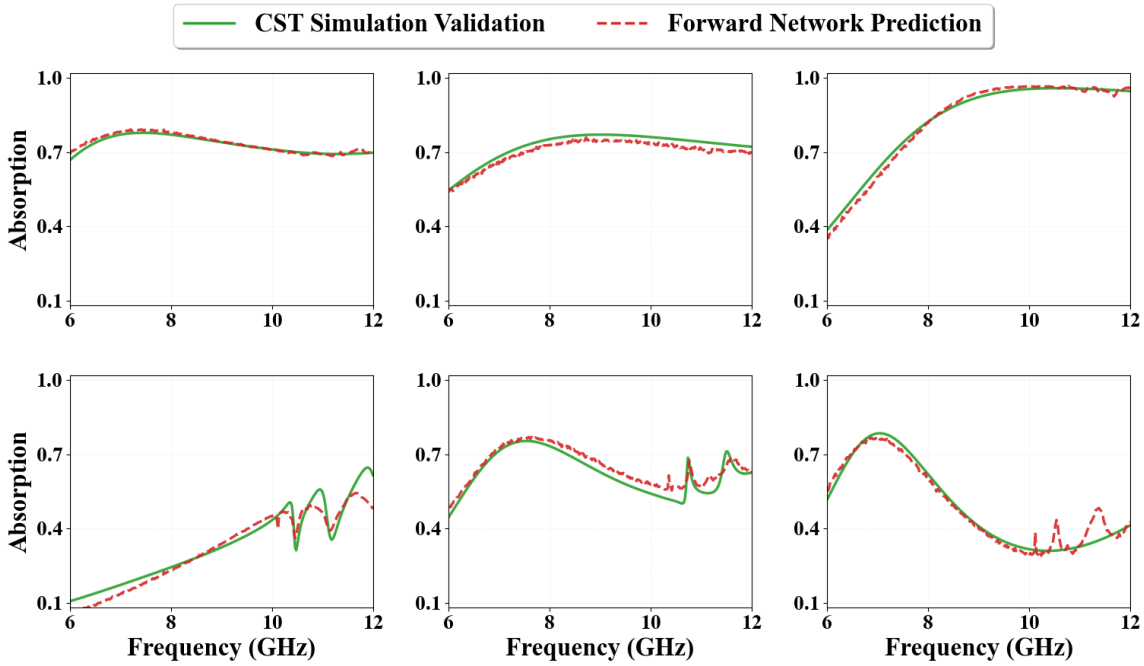

FIGURE 5. Predictions of forward prediction DNN.

tion is high or low, stable or rapidly varying, the forward network consistently delivers accurate predictions.

3.3. Inverse Design Deep Neural Network

After completing the design of the forward network, the inverse design network was designed, as shown in Fig. 6. The network input consists of the electromagnetic response (absorption performance) and angle parameters (incident angle θ), while the output comprises the structural parameters ($P, R1, R2, R3$) and material parameters ($r1, r2$).

The loss curve during inverse network training is shown in Fig. 4(b), where the loss gradually decreases and stabilizes as learning progresses. The inverse neural network has five hidden layers, each containing 512 neurons. The final test loss of the inverse network was 0.0067.

A target electromagnetic response was randomly selected and input into the tandem network. The inverse network rapidly generated the corresponding structural design of the metasurface absorber. Meanwhile, the trained forward network output the predicted electromagnetic response, enabling performance evaluation of the inversely designed unit cell. To further validate the accuracy of the network-generated designs, full-wave simulations were performed in CST using the structural parameters predicted by the inverse network. The simulated responses show excellent agreement with both the target and the forward network predictions. As shown in Fig. 7, the inverse network can effectively generate unit cell structures that achieve the target performance, with the CST validation confirming the reliability of the inverse design framework.

4. SCATTERING SUPPRESSION BASED ON ANGULAR SENSITIVITY

When a non-planar object is illuminated by electromagnetic waves, its geometric shape gives rise to scattering character-

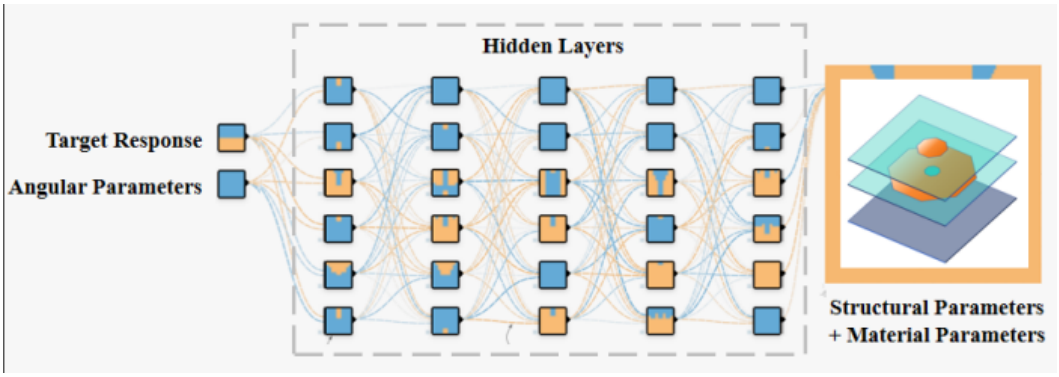

FIGURE 6. Inverse design DNN.

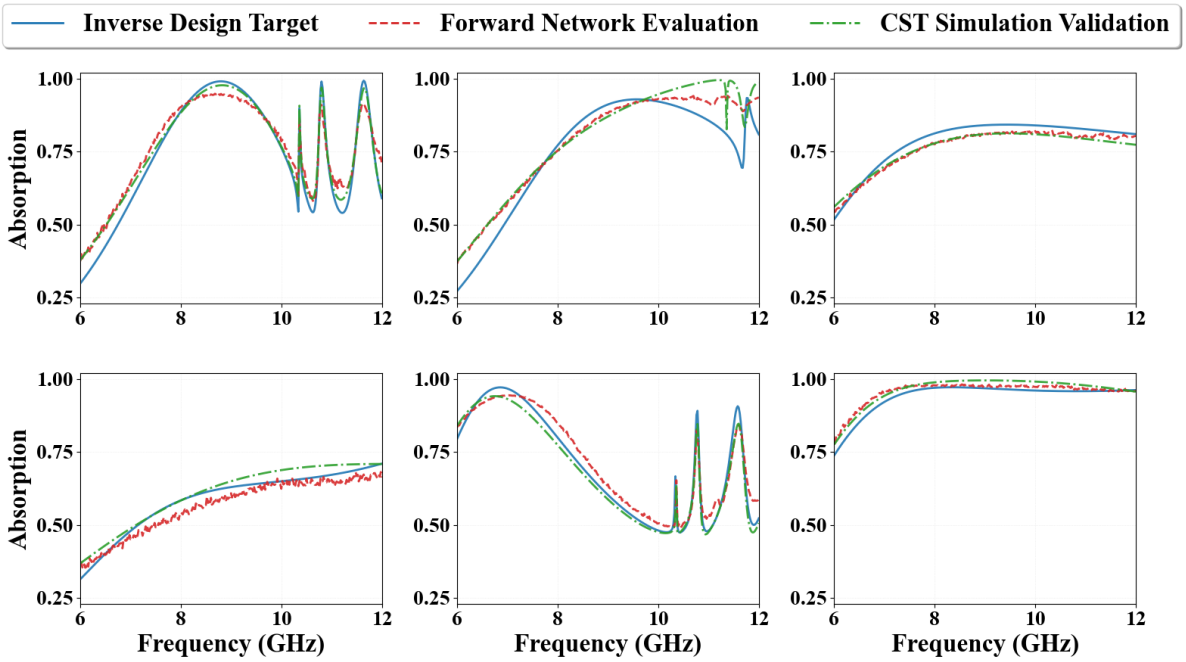

FIGURE 7. Predictions of the tandem deep neural network.

istics along multiple primary directions. To address this, we propose a strategy that combines geometric considerations with angular-specific unit cell design. By tailoring unit cells for the incident angles corresponding to primar y detection directions, omnidirectional scattering suppression can be achieved. Two scenarios were selected to validate this approach.

4.1. Case 1: Hybrid Structure Design at 10.4 GHz

Using the simplified case shown in Fig. 8 as the study platform, electromagnetic waves propagate along the negative Z-axis with the electric field polarized along the positive Y-axis. In this case, the waves impinge upon two planes of a PEC object with different inclinations: normal incidence occurs on the right plane relative to the Y-axis, while a 50° incident angle is observed on the left plane ($\alpha 1 = 50°$). The operating frequency is set to 10.4 GHz.

A hybrid arrangement based on angular-selective absorbers was proposed for this configuration. The right region under normal incidence employs a near-angle metasurface absorber inversely designed for vertical incidence, while the left region with 50° incidence adopts a large-angle absorber structure optimized for oblique illumination.

The target responses shown in Fig. 9 were input into the inverse design network at incident angles of 0° and 50°, respectively. The resulting absorber unit cell structures are presented in Fig. 10, with the corresponding design parameters listed in Table 1.

The S_{11} performance of the two unit cells at 10.4 GHz exhibits a significant contrast under normal and oblique incidence, as shown in Fig. 11. Unit Cell 1, designed for normal incidence, achieves strong absorption (-36.42 dB) at 0° but performs poorly (-9.98 dB) at 50°. In contrast, Unit Cell 2, optimized for oblique incidence, delivers excellent absorption (-29.32 dB) at 50° while showing limited absorption

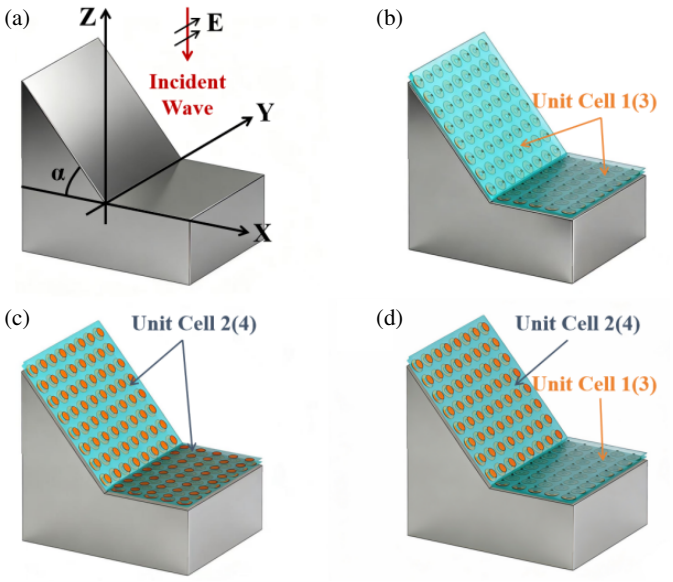

FIGURE 8. Schematic diagram of the proposed configuration under normal incidence and oblique incidence at an angle α. (a) The PEC reference structure 1 (for $\alpha 1$)/2 (for $\alpha 2$). (b) Control group 1 (for $\alpha 1$)/3 (for $\alpha 2$), (c) Control group 2 (for $\alpha 1$)/4 (for $\alpha 2$), and (d) the hybrid optimized group 1 (for $\alpha 1$)/2 (for $\alpha 2$), all in the same coordinate system.

TABLE 1. Design parameters of the generated unit cells.

Unit Cell	P (mm)	$R1$ (mm)	$R2$ (mm)	$R3$ (mm)	$r1$ (Ω/sq)	$r2$ (Ω/sq)
1	15	1.0	6.0	2.0	50	50
2	15	4.0	6.0	3.0	50	50

(−11.34 dB) under normal illumination. This pronounced angular selectivity confirms that each unit cell is effectively tailored to its target incident angle by the inverse design network.

To elucidate the physical mechanisms underlying the distinct angular sensitivities of the two designed absorbers, we examine their surface current and surface power loss density under both normal (0°) and oblique (50°) incidence, as shown in Fig. 12.

Unit 1 exhibits strong absorption at 0° (99.8%, $S_{11} = -36.42$ dB) but weak absorption at 50° (68%, $S_{11} = -9.98$ dB). At 0°, the currents on the top and middle ITO layers both flow upward, while the bottom metal current flows downward, forming a circulating current distribution characteristic of magnetic resonance. The power loss density is predominantly distributed symmetrically in the middle ITO layer, indicating that conduction current dominates energy dissipation. At 50°, the in-plane wavevector component introduced by oblique incidence breaks the structural symmetry, inducing an x-component in the currents and converting part of the current into displacement current (which does not generate Joule heating), while the overall current intensity decreases.

Importantly, the top and middle ITO currents become opposite in direction, weakening the coherence of the circulating current distribution. Although the middle and bottom layers still maintain opposite directions, the magnetic resonance is degraded. Thus, the absorption at 0° far surpasses that at 50°, which constitutes the essence of the angle-sensitive behavior of Unit 1.

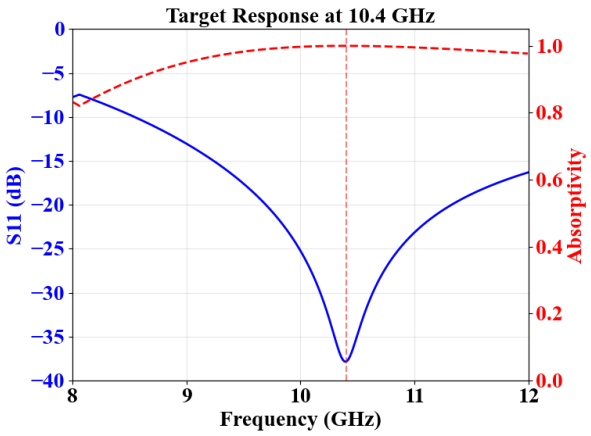

FIGURE 9. Target response of the metasurface absorber at 10.4 GHz under different incident angles. The displayed frequency range is cropped to highlight the absorption peak; the complete operating band of the network is 6–12 GHz.

Unit 2 exhibits the opposite trend: weak absorption at 0° (73%, $S_{11} = -11.34$ dB) but strong absorption at 50° (99.9%, $S_{11} = -29.32$ dB). At 0°, the top current flows upward, while the middle ITO layer exhibits a vortex-like current distribution that prevents the formation of a coherent circulating pattern with the top and bottom layers. The bottom current flows downward, yet the disorder in the middle layer hinders the establishment of magnetic resonance. Power loss appears only as isolated hot spots in the middle layer, resulting in overall weak absorption. At 50°, the transverse wave vector of the oblique incidence compensates the phase mismatch, aligning the top and middle ITO currents in-phase (both downward) and reversing the bottom current to upward, thereby creating a strong circulating current distribution. The currents become highly concentrated along the central edges, and the power loss forms a continuous high-loss band, dramatically increasing the total absorbed power. Unit 2 thus undergoes a "switch-like" transition from a vortex-dominated, displacement-current-prone state at 0° to a conduction-current-dominated magnetic resonance at 50°, which is the essence of its angle-sensitive behavior.

To better validate the scattering suppression enabled by the targeted design of angular-sensitive metasurfaces, four configurations were simulated to evaluate the absorption performance of the metasurface absorber in the simplified hybrid case 1:

- The PEC reference group 1, consisting of a bare metal surface without any absorber (Fig. 8(a));
- Control group 1, fully covered with Unit Cell 1 (Fig. 8(b));
- Control group 2, fully covered with Unit Cell 2 (Fig. 8(c));
- The hybrid optimized group 1, featuring a composite structure with both Unit Cell 1 and Unit Cell 2 (Fig. 8(d)).

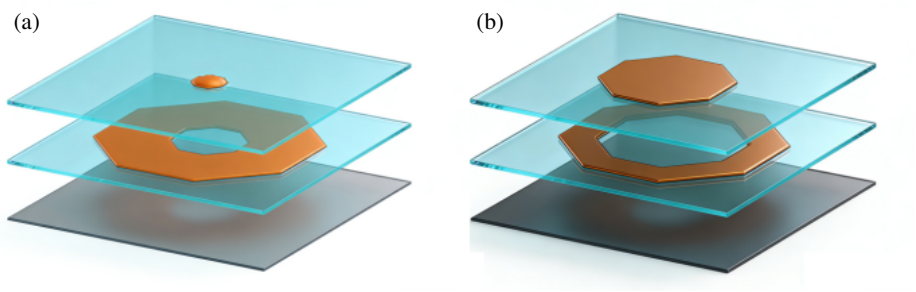

FIGURE 10. Schematic of unit cell structures generated by the inverse network: (a) Unit cell 1 with an input incident angle of 0°; (b) Unit cell 2 with an input incident angle of 50°.

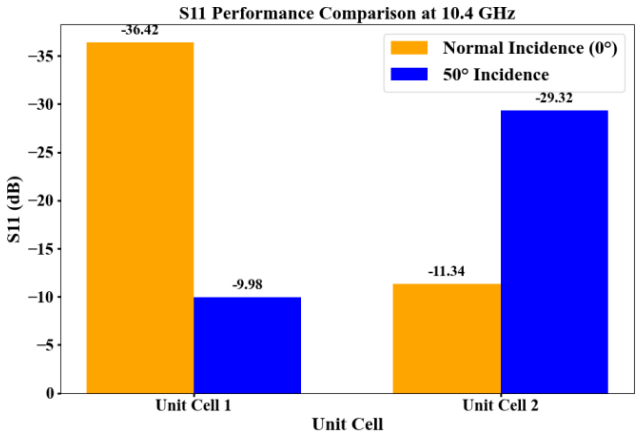

FIGURE 11. S_{11} performance comparison of the two inversely designed unit cells under normal (0°, Unit Cell 1) and oblique (50°, Unit Cell 2) incidence at 10.4 GHz.

RCS calculations were performed for the four configurations using simulation software, with results shown in Fig. 13(a). The blue curve represents the RCS of the bare metal surface without any absorber, where strong scattering occurs in multiple directions.

From the RCS results of control groups 1 and 2, it can be observed that control group 1, covered with the normally-incident designed metasurface absorber (Unit Cell 1), exhibits significantly lower RCS (orange curve) in the near-axis region ($-20°$ to 20°) than control group 2 (green curve), indicating superior scattering suppression capability in the near-axis direction. As the scattering angle increases, the performance comparison reverses: control group 2, covered with the 50°-incident designed metasurface absorber (Unit Cell 2), shows substantially lower RCS (green curve) in the large-angle scattering region ($-60°$ to $-90°$) than control group 1 (orange curve), demonstrating better suppression effectiveness for large-angle scattering side lobes.

When the RCS results of the hybrid experimental group (red curve) are included for comparison, this group effectively combines the advantages of both control groups through targeted hybrid deployment. It achieves scattering suppression comparable to control group 1 in the near-axis region while maintaining suppression effectiveness similar to control group 2 in the large-angle scattering region. Consequently, RCS reduction is achieved across the entire angular range, demonstrating superior comprehensive absorption performance.

To evaluate the angular robustness of the hybrid structure, we examined its scattering performance under oblique incidence. Taking the 50° case as an example, Figs. 13(b)–(c) shows the results when the incident angle deviates by $\pm 5°$. It can be seen that the hybrid configuration maintains a stable omnidirectional scattering suppression advantage across this small angular range. This behavior is partly attributed to the inherent robustness of the individual unit cells.

4.2. Case 2: Hybrid Structure Design at 7.8 GHz

For the second case study, the verification model remains the one depicted in Fig. 8(a) with $\alpha 2 = 30°$. All other conditions remain the same.

The target responses input into the inverse design network are shown in Fig. 14, with incident angles set to 0° and 30°, respectively. Unit Cell 3 and Unit Cell 4 were obtained through the inverse design network, and their structural parameters are listed in Table 2.

TABLE 2. Design parameters of the generated unit cells.

Unit Cell	P (mm)	$R1$ (mm)	$R2$ (mm)	$R3$ (mm)	$r1$ (Ω/sq)	$r2$ (Ω/sq)
3	15	2.6	7.0	1.9	50	50
4	15	3.5	7.0	1.5	50	50

Similar to Case 1, the S_{11} performance of the two unit cells at 7.8 GHz exhibits pronounced angular selectivity, as shown in Fig. 15. Unit Cell 3, designed for normal incidence, achieves strong absorption (-36.74 dB) at 0° but performs poorly (-20.37 dB) at 30°. In contrast, Unit Cell 4, optimized for 30° incidence, delivers excellent absorption (-44.58 dB) at 30° while showing limited absorption (-20.74 dB) under normal illumination. This angular-selective behavior confirms that each unit cell is effectively tailored to its target incident angle by the inverse design network, consistent with the observations in Case 1.

Four configurations were simulated to evaluate the absorption performance of the metasurface absorber in the simplified hybrid Case 2:

- The PEC reference group 2, consisting of a bare metal surface without any absorber (Fig. 8(a));

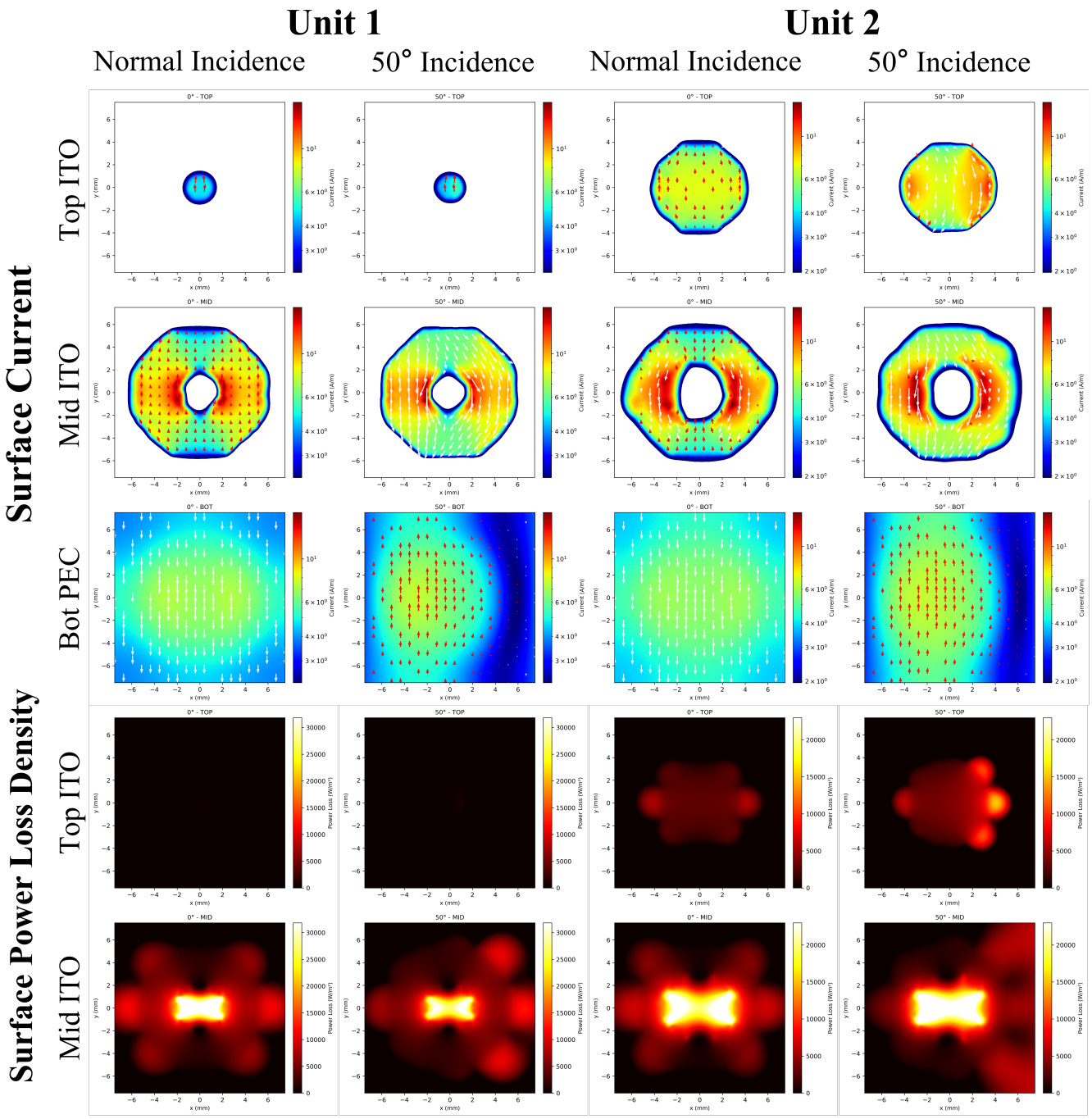

FIGURE 12. Simulated surface current and surface power loss density distributions for Unit 1 and Unit 2 at 0° and 50° incidence at 10.4 GHz. The arrows indicate the direction of the surface current (real part), with red and white colors denoting positive and negative y-components, respectively. All plots share the same spatial coordinates (x, y), and the incident direction is along the positive x-axis (TE polarization).

- Control group 3, fully covered with Unit Cell 3 (Fig. 8(b));
- Control group 4, fully covered with Unit Cell 4 (Fig. 8(c));
- The hybrid optimized group 2, with Unit Cell 3 and Unit Cell 4 (Fig. 8(d)).

Following the same analysis approach as Case 1, the RCS results for the four configurations in Case 2 are shown in Fig. 16. The blue curve represents the PEC reference group 2 (bare metal surface with horizontal and 30° sloped surfaces), where strong scattering occurs in multiple directions.

When the RCS results of the hybrid optimized group 2 (red curve) are examined, this group effectively combines the responses of both control units through targeted deployment, with Unit Cell 3 on the horizontal plane and Unit Cell 4 on the 30° sloped surface. The hybrid configuration achieves scattering suppression that closely follows the superior performance of Unit Cell 4 across the entire angular range. This indicates that

TABLE 3. Comparison of recent metasurface absorber design approaches.

Reference	Ref. [31]	Ref. [32]	Ref. [33]	This work
Research Target	Magnetic Absorbers	Angular-stable Absorbers	Transparent Absorbers	Omnidirectional scattering suppression via angular-selective absorbers
Design Method	Neural network-based permittivity engineering	Parametric sweep/ equivalent circuit	Multi-layer ITO grid optimization	Tandem deep neural network
Key Achievement	−45.12 dB at 5.16 GHz with 1.9 mm Thickness	30° (TE)/60° (TM) angular stability	45° angular stability	Omnidirectional scattering suppression from −90° to 50° via hybrid arrangement
Research Innovation	Physics-informed neural network for material selection strategy	Novel 3D structure with experimental validation	ITO-based transparent absorber with angular stability	Exploiting angular sensitivity for scattering suppression with deep learning-enabled rapid design

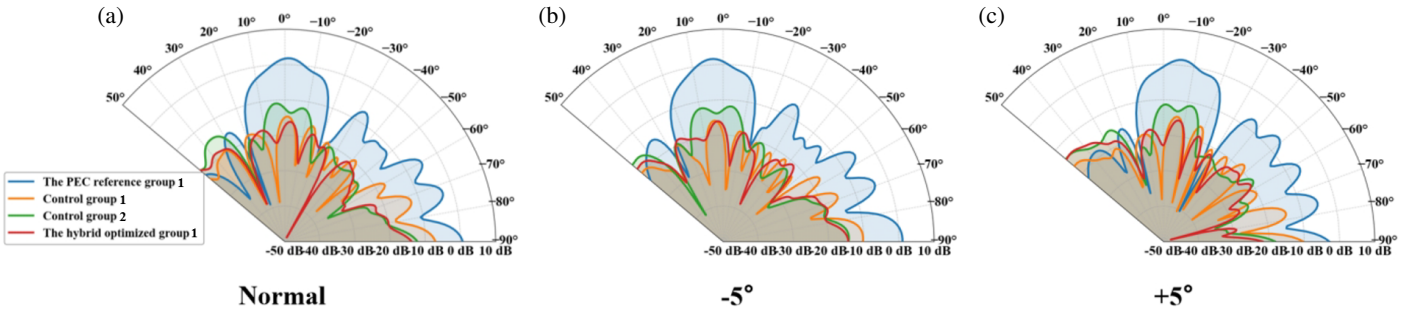

FIGURE 13. RCS results (a) under normal incidence, (b) at −5° incidence, and (c) at +5° incidence.

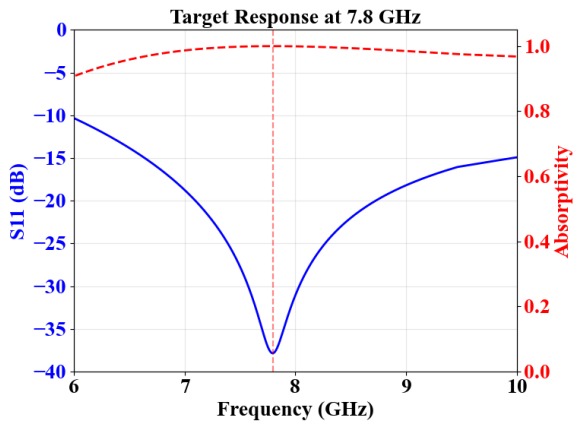

FIGURE 14. Target response of the metasurface absorber at 7.8 GHz under different incident angles. The displayed frequency range is cropped to highlight the absorption peak; the complete operating band of the network is 6–12 GHz.

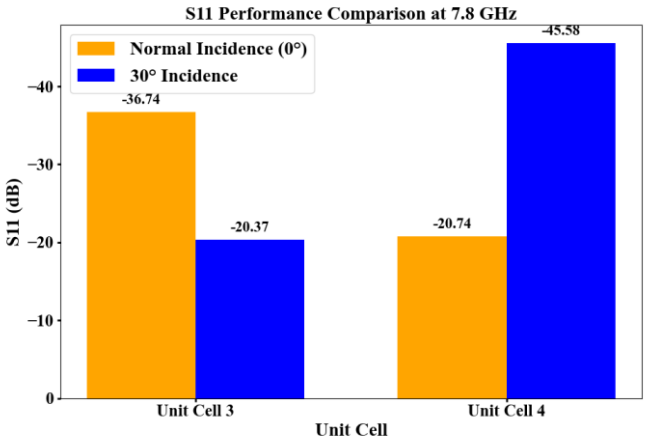

FIGURE 15. S_{11} performance comparison of the two inversely designed unit cells under normal (0°, Unit Cell 3) and oblique (30°, Unit Cell 4) incidence at 7.8 GHz.

the joint structure effectively inherits the response characteristics of the better-performing unit, leading to comprehensive RCS reduction. These results are consistent with the observations from Case 1, further validating the effectiveness and generalizability of the proposed hybrid design strategy for omnidirectional scattering reduction.

As shown in Table 3, this work is different from previous studies in research concept and design method. Ref. [31] uses a physics-informed neural network to design magnetic absorbers at the material level, together with practical experience to guide material fabrication. Refs. [32] and [33] focus on achieving angular-stable absorbers using parametric sweeps or equivalent circuit methods.

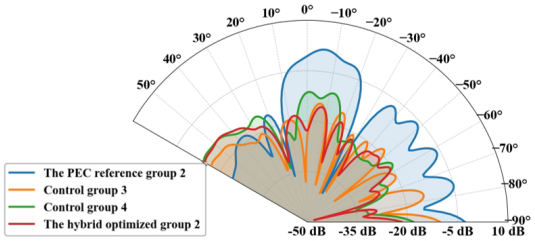

FIGURE 16. RCS results under normal incidence.

In contrast, this work takes a different approach. Instead of trying to avoid angular sensitivity — as in angular stable absorber designs — we use it as a design tool. By designing unit cells with different angular responses based on the shape of real objects, we achieve omnidirectional scattering suppression from $-90°$ to $40°$. To handle the design complexity of hybrid configurations, we use a tandem deep neural network for fast inverse design. This greatly simplifies the design process compared to traditional parametric sweeps. This change from avoiding to using angular sensitivity, together with deep learningbased fast design, provides a new way to control the angular response of metasurfaces for real stealth applications.

5. CONCLUSION

Artificial intelligence has strongly promoted the development and application of metasurface technology. Intelligent design using neural networks and optimization algorithms has become an important direction for metasurface research. In this work, a tandem neural network is adopted for the inverse design of metasurface absorbers. The forward network acts as an efficient alternative to full-wave simulations and enables fast electromagnetic response prediction. The inverse network, trained in tandem with the frozen forward network, builds a performance-driven design framework that breaks the limits of conventional structure-dependent and manual-tuning methods. A complete T-DNN design workflow is established, offering a practical method for inverse design of metasurfaces and related devices.

Furthermore, this study explored the possibility of designing absorbers with different angular responses based on different geometric features. The ITO-based absorbers employed in this work offer practical advantages, including ease of fabrication, convenient integration with hybrid structures, and relatively low cost, making them well-suited for demonstrating design methodologies intended for real-world applications. By combining two types of absorbers, sidelobe scattering was effectively reduced while maintaining mainlobe suppression capability, leading to more uniform omnidirectional scattering reduction. This system-level design strategy — leveraging multi-angle sensitivity to achieve omnidirectional scattering suppression — represents a conceptual shift from designing individual structures to engineering composite configurations that harness angular diversity. Combined with neural network-based inverse design, this approach shows good potential for multi-angle electromagnetic wave control. The synergy between the application-driven design concept and the efficiency of deep learning inverse design forms a practical pathway for implementing complex hybrid configurations that would be challenging to realize through traditional parametric sweeps.

Several aspects of this study need further investigation. Future work will explore the use of new neural network structures in metasurface design and optimization, analyze the physical mechanism of angular sensitivity and the interactions between multiple structures. Experimental validation of the designed absorbers will also be conducted to further verify the simulation results and demonstrate the practical feasibility of the proposed approach. With the help of artificial intelligence methods, further efforts will be made to optimize the spatial arrangement and combination strategies of absorbers to improve overall absorption and scattering suppression performance and to promote the application of this technology in practical scenarios.

ACKNOWLEDGEMENT

National Key Research and Development Program of China (Grant Nos. 2022YFA1404704 and 2022YFA1405201); National Natural Science Foundation of China (Grant Nos. 62475228 and U25A20520); National Ten Thousand Talent Program — Young Top-notch Talent Project; Fundamental Research Funds for the Central Universities (Grant No. 226-2024-00125); Key Research and Development Program of Zhejiang Province (Grant No. 2024C01160); Science and Technology Program of Jinhua City (Grant Nos. 2024-1-077 and 2026-1-026).

REFERENCES

[1] Tan, D., C. Jiang, Q. Li, S. Bi, X. Wang, and J. Song, "Development and current situation of flexible and transparent EM shielding materials," *Journal of Materials Science: Materials in Electronics*, Vol. 32, No. 21, 25 603–25 630, 2021.

[2] Cheng, Y., Y. Zou, H. Luo, F. Chen, and X. Mao, "Compact ultra-thin seven-band microwave metamaterial absorber based on a single resonator structure," *Journal of Electronic Materials*, Vol. 48, No. 6, 3939–3946, 2019.

[3] Abdulkarim, Y. I., A. Mohanty, O. P. Acharya, B. Appasani, M. S. Khan, S. K. Mohapatra, F. F. Muhammadsharif, and J. Dong, "A review on metamaterial absorbers: Microwave to optical," *Frontiers in Physics*, Vol. 10, 893791, 2022.

[4] Hsiao, H.-H., C. H. Chu, and D. P. Tsai, "Fundamentals and applications of metasurfaces," *Small Methods*, Vol. 1, No. 4, 1600064, 2017.

[5] Tian, Y., J. Jin, H. Yang, L. Fan, J. Hou, and H. Lin, "Research progress on design and application of microwave electromagnetic metamaterial," *SCIENTIA SINICA Physica, Mechanica & Astronomica*, Vol. 53, No. 9, 290016, 2023.

[6] Chen, H., B.-I. Wu, B. Zhang, and J. A. Kong, "Electromagnetic wave interactions with a metamaterial cloak," *Physical Review Letters*, Vol. 99, No. 6, 063903, 2007.

[7] Cai, T., B. Zheng, J. Lou, L. Shen, Y. Yang, S. Tang, E. Li, C. Qian, and H. Chen, "Experimental realization of a superdispersion-enabled ultrabroadband terahertz cloak," *Advanced Materials*, Vol. 34, No. 38, 2205053, 2022.

[8] Pan, M., Y. Fu, M. Zheng, H. Chen, Y. Zang, H. Duan, Q. Li, M. Qiu, and Y. Hu, "Dielectric metalens for miniaturized imaging systems: Progress and challenges," *Light: Science & Appli-*

cations, Vol. 11, No. 1, 195, 2022.

[9] Bukhari, S. S., J. Vardaxoglou, and W. Whittow, "A metasurfaces review: Definitions and applications," *Applied Sciences*, Vol. 9, No. 13, 2727, 2019.

[10] Zhou, W., S. Zhu, Z. Zhang, R. Zhu, B. Chen, J. Zhao, X. Wei, H. Lu, and B. Zheng, "Time-varying metasurface driven broadband radar jamming and deceptions," *Optics Express*, Vol. 32, No. 10, 17 911–17 921, 2024.

[11] Yuan, Y., W. Zhou, R. Wang, Y. Wang, Y. Dong, S. N. Burokur, and K. Zhang, "Non-orthogonal metasurfaces for channel-locked spin-orbital transitions," *Advanced Photonics*, Vol. 7, No. 5, 056009, 2025.

[12] Li, J., A. Jana, Y. Yuan, K. Zhang, S. N. Burokur, and P. Genevet, "Exploiting hidden singularity on the surface of the Poincaré sphere," *Nature Communications*, Vol. 16, No. 1, 5953, 2025.

[13] Lu, H., J. Zhao, B. Zheng, C. Qian, T. Cai, E. Li, and H. Chen, "Eye accommodation-inspired neuro-metasurface focusing," *Nature Communications*, Vol. 14, No. 1, 3301, 2023.

[14] Landy, N. I., S. Sajuyigbe, J. J. Mock, D. R. Smith, and W. J. Padilla, "Perfect metamaterial absorber," *Physical Review Letters*, Vol. 100, No. 20, 207402, 2008.

[15] Lei, X., S. Huo, Y. Li, M. Wang, Z. Sun, H. Yu, and E. Li, "Design of miniaturized metamaterial absorber and analysis of electromagnetic absorption mechanism," *Chinese Journal of Radio Science*, Vol. 36, No. 6, 896–904, 2021.

[16] Ning, R. X., F. Wang, J. L. Lu, L. Y. Li, Q. L. Ren, and Z. Jiao, "A large angle tunable triple-band metamaterial absorber," *Chinese Journal of Radio Science*, Vol. 38, No. 3, 548–554, 2023.

[17] Wu, R. K., B, He, K. Zang, M. Wang, H. X. Zheng, and C. Fan, "Metamaterial wave absorbers based on tin disulfide/reduced graphene oxide," *Journal of Hebei University of Technology*, Vol. 53, No. 5, 39–46, 2024.

[18] Ding, F., Y. Cui, X. Ge, Y. Jin, and S. He, "Ultra-broadband microwave metamaterial absorber," *Applied Physics Letters*, Vol. 100, No. 10, 103506, 2012.

[19] Zhang, Q., Z. Shen, J. Wang, and K. S. Lee, "Design of a switchable microwave absorber," *IEEE Antennas and Wireless Propagation Letters*, Vol. 11, 1158–1161, 2012.

[20] Zhu, W., F. Xiao, M. Kang, and M. Premaratne, "Coherent perfect absorption in an all-dielectric metasurface," *Applied Physics Letters*, Vol. 108, No. 12, 121901, 2016.

[21] Lu, H., J. Zhao, P. Zhu, W. Song, S. Zhu, R. Zhu, B. Zheng, and H. Chen, "Neural network-assisted metasurface design for broadband remote invisibility," *Advanced Functional Materials*, Vol. 35, No. 45, 2506085, 2025.

[22] Zhao, J., P. Zhu, Z. Wen, F. Tang, B. Zheng, R. Zhu, H. Qian, C. Qian, H. Lu, and H. Chen, "Adaptive transparent cloaking tunnel enabled by meta-reinforcement-learning metasurfaces," *PhotoniX*, Vol. 7, No. 1, 2, 2026.

[23] Zhao, J., Q. Yu, B. Qian, K. Yu, Y. Xu, H. Zhou, and X. Shen, "Fully-decoupled radio access networks: A resilient uplink base stations cooperative reception framework," *IEEE Transactions on Wireless Communications*, Vol. 22, No. 8, 5096–5110, 2023.

[24] Lu, H., C. Luo, Z. Pei, P. Zhu, Y. Dong, C. Chen, R. Zhu, and J. Zhao, "FlexSARCloak: A flexible SAR cloak driven by task-oriented learning," *ACS Applied Materials & Interfaces*, Vol. 17, No. 1, 2139–2147, 2025.

[25] Shuang, Y., L. Li, Z. Wang, M. Wei, and L. Li, "Metasurface-assisted intelligent electromagnetic sensing: Theory, design and experiment," *Chinese Journal of Radio Science*, Vol. 36, No. 6, 858–866, 2021.

[26] Li, L., H. Zhao, C. Liu, L. Li, and T. J. Cui, "Intelligent metasurfaces: Control, communication and computing," *eLight*, Vol. 2, No. 1, 7, 2022.

[27] Ma, J., M. Wang, H. Zheng, and E. Li, "Research on a deep neural network-based prediction method for metamaterial absorbers," *Chinese Journal of Radio Science*, Vol. 40, No. 3, 494–502, 2025.

[28] Huang, M., B. Zheng, R. Li, X. Li, Y. Zou, T. Cai, and H. Chen, "Diffraction neural network for multi-source information of arrival sensing," *Laser & Photonics Reviews*, Vol. 17, No. 10, 2300202, 2023.

[29] Zhen, Z., C. Qian, Y. Jia, Z. Fan, R. Hao, T. Cai, B. Zheng, H. Chen, and E. Li, "Realizing transmitted metasurface cloak by a tandem neural network," *Photonics Research*, Vol. 9, No. 5, B229–B235, 2021.

[30] Qian, C., B. Zheng, Y. Shen, L. Jing, E. Li, L. Shen, and H. Chen, "Deep-learning-enabled self-adaptive microwave cloak without human intervention," *Nature Photonics*, Vol. 14, No. 6, 383–390, 2020.

[31] Liu, C., J. Li, S. Li, Z. Guo, Y. Chen, T. Li, R. Qin, J. Sun, Y. Lu, and F. Meng, "Neural network-based permittivity engineering of magnetic absorbers for customizable microwave absorption," *Advanced Science*, e21945, 2026.

[32] Tiwari, G., P. K. Gupta, T. Kumar, and B. Mukherjee, "A novel three-dimensional broadband angular stable polarization insensitive microwave metamaterial absorber," *Physica Scripta*, Vol. 100, No. 7, 075527, 2025.

[33] Wu, Y., C. Fu, Y. Jiang, J. Bian, and W. Gu, "Angle-insensitive broadband transparent microwave absorber with high shielding effectiveness," *Optics Letters*, Vol. 50, No. 2, 459–462, 2025.